Precision Engineering 90 (2024) 176–190

Contents lists available at ScienceDirect

Precision Engineering

journal homepage: www.elsevier.com/locate/precision

Exploring three-dimensional photoinhibition to enhance vat photopolymerization: A preliminary study

Yue Zhang, Heyang Zhang, Xiayun Zhao [*]

ZXY Intelligent Precision – Advanced Manufacturing (ZIP-AM) Laboratory, Department of Mechanical Engineering and Materials Science, University of Pittsburgh, Pittsburgh, PA, 15261, USA

ARTICLE INFO

Handling Editor: Prof. R. Leach

Keywords:
Additive manufacturing
Vat photopolymerization
Photoinhibition
Over-curing
Pillar array

ABSTRACT

Vat photopolymerization (VPP) based additive manufacturing (AM) technologies print 3D components by using light to selectively cure photosensitive resins. In VPP-based AM, one outstanding challenge remains in controlling the over-curing, which is mainly caused by the diffusive and/or excessive photo-induced species such as free radicals and can severely affect the geometric properties of as-printed parts. Common practices rely on formulating proper resins or optimizing exposure parameters to address the vertical over-curing but often ignore the lateral over-curing. In this work, we develop a new VPP process of photoinhibition aided photopolymer AM (PinPAM) to comprehensively address over-curing issues in both vertical and lateral dimensions for enhancing the properties of as-printed geometry. The PinPAM method incorporates an adaptive photoinhibition zone, generated both surrounding and underneath the curing zone on a layer basis. This differs from current literature approaches that utilize photoinhibition to create a higher deadzone to increase print speed or constrain vertical profiles for achieving volumetric VPP AM. We present several preliminary experimental study cases involving pillar array sample printing. By comparing part dimensions and shapes resulting from traditional VPP and PinPAM, our experiments prove the concept of PinPAM and demonstrate its potential to address over-curing in VPP. Furthermore, we present an initial case study on optimizing the PinPAM process for printing cylinder samples with targeted dimensions, illustrating the planning and implementation of PinPAM. A discussion on future research directions to establish PinPAM is included. The developed PinPAM opens up a new avenue for improving VPP printed parts' geometrical properties and facilitating its adoption in precision fabrications that demand dimensional accuracy and resolution.

1. Introduction

Additive manufacturing (AM) can process a wide spectrum of materials including metals, polymers, and ceramics, to form complex structures and useable parts in various industries such as aerospace, automotive, energy and medical. AM has grown rapidly in recent years with huge economic impacts. The worldwide revenues from AM material sales alone exceeded 900 million US dollars in 2016, with photopolymers occupying 39 % due to their dominant mature AM applications in prototyping and molding [1]. Even though metals and other polymers AM have been gaining increasing industry adoption, photopolymer remains as the most widely used material class for AM and will embrace more appealing applications, especially with the development of AM processes and functional polymers for bioprinting and 4D printing [2–4]. Vat photopolymerization (VPP) AM offers a promising fabrication technique to make complex-shaped and functional components with soft materials such as hydrogels and polymers in applications of tissue engineering, flexible electronics, and soft robotics [5].

Recent advances in VPP include the inkjet printing of UV-curable functional inks for fabricating electronics [6,7], the continuous liquid interface production (CLIP) that combines photopolymerization with oxygen inhibition induced dead-zone [8], and a volumetric AM technology of printing 3D polymer structures using 3D projection in one shot [9]. These cutting-edge technologies have advantages in printing speed but still face issues with printed geometry, such as inadequate resolution, precision, and accuracy [10–13]. The most precise VPP that can create three-dimensional submicron features is based on the two-photon polymerization (TPP) process [14–18], which, however, is too expensive and has drawbacks of limited printing speed, constrained build volume, and complicated implementation. To push forward the advancement

---

* Corresponding author.
E-mail address: xiayun.zhao@pitt.edu (X. Zhao).

https://doi.org/10.1016/j.precisioneng.2024.08.009
Received 8 May 2024; Received in revised form 10 August 2024; Accepted 19 August 2024

and adoption of VPP for the aforementioned industries, there is an urgent need for a cost-effective and high-throughput VPP technology that can print parts with geometric accuracy and precision.

One outstanding challenge in VPP-based AM (VPP-AM) is over-curing, which manifests as geometrical deviations, particularly in dimensions exceeding expectations. In general, over-curing is the solidification of additional resin outside of the target cross-section due to uncured resin (residing in and surrounding the printed layers) being cured by excess crosslinking species (e.g., radicals in free-radical VPP), which are either induced by light scattering and penetration or simply the diffusion of those species [19]. In VPP-AM it is well known that the light penetrating through printed layers could cause significant over-curing in the vertical or buildup direction, often referred to as “cure-through” [20]. With an appropriate amount of vertical over-curing, interlayer bonding can be established to join the printed layer and avoid delamination [21]. However, too much vertical over-curing tends to affect the printed geometry. To decrease the vertical over-curing, the commonly used method is adjusting resin formulation to decrease the light penetration depth by selecting proper non-reactive light absorbers and/or modulating their concentration [22–24]. However, this method decreases the penetration depth at the cost of print speed. Another method is to optimize the printing parameters. Some researchers have developed models to simulate the energy dose during printing by modulating the pixel grayscale value of the projected image. This approach aims to tune the dose profile to minimize vertical over-curing [25–27]. However, this grayscale method may be limited in its ability to achieve the desired strength of the cured part, leading to potential issues with under-curing while attempting to reduce over-curing. A recent paper reports an in-situ transfer VPP (IsT-VPP) process to prevent light penetration into the residual liquid resin inside the target channel by using a main platform to print the upper part of the channel and an auxiliary platform to print the lower part, respectively. The two-channel parts are in-situ assembled by secondary exposure curing [28]. Despite its applicability to general resins and machines, such a process is limited in print speed, printable geometry (simple designs such as channels), and geometry accuracy (needing alignment of separate platforms and parts). Moreover, the IsT-VPP is developed to control over-curing in the depth direction only.

As current methods focus on addressing the vertical over-curing, scarce research has been done to suppress the over-curing effect in the lateral direction (perpendicular to the build direction). The optical system parameters (e.g., digital micromirror size and pitch, magnification factor) critically determine the projected image quality (e.g., pixel size, image blurring and distortion) [29], thus defining a theoretical limit of achievable lateral accuracy and resolution for VPP processes. However, in the practice of VPP-AM, it is still a challenge to reach the theoretical resolution determined by the inherent optical system characteristics due to lateral over-curing [13]. To improve lateral resolution, researchers have demonstrated that optimizing the projection light intensity in terms of grayscale values rather than binary intensity could help refine the lateral dimensions but at a cost of mechanical strength. To conclude, there still lacks an agile and continuous process to comprehensively tackle both the vertical and lateral over-curing while printing various complex geometries in VPP.

In this work, we report a proof-of-concept study on developing a new VPP process, referred to as photoinhibition aided photopolymer AM (PinPAM), whereby an adaptive photoinhibition zone that contains the curing zone from not only beneath but also surrounding will be generated on a layer basis. A few current literature methods also use photoinhibition [30–32], however, to increase the print speed of VPP by using vertical photoinhibition to generate a higher dead-zone or confine the vertical profiles for realizing a volumetric VPP process. By contrast, our PinPAM method features employing layer-wise geometry-aware photoinhibition and photopolymerization optical masks that can be optimized at the pixel level to prevent lateral over-curing while attaining the desired vertical thickness in the printed parts. PinPAM is demonstrated to have great potential for comprehensively addressing the over-curing issues at both lateral and vertical dimensions and thus improving the geometrical properties (dimensional accuracy, resolution, feature size) of VPP printed parts.

The remaining paper is organized to begin with an introduction to our PinPAM system and materials in Section 2, followed by a proof-of-concept study in Section 3 to evaluate the capability of PinPAM process in enhancing geometrical accuracy and precision. Furthermore, Section 4 demonstrates the PinPAM process planning method based on multi-objective optimization with a preliminary case study of optimizing inhibition light intensity values for printing a cylindrical sample with both accurate height and diameter. Section 5 provides our conclusions and recommendations for future work to improve PinPAM.

2. Experiment system

2.1. PinPAM system setup

As shown in Fig. 1, our prototyping PinPAM system comprises an assembly of two-wavelength mask projection optics (PRO4500, Wintech Digital, Carlsbad, CA) that can provide patterned light beams (blue light: 460 nm; ultraviolet (UV) light: 365 nm) for polymerization and inhibition, respectively. It also includes a vertically movable precision platform driven by a micro-linear stage (LTS 150, Thorlabs, NJ). An in-house LabVIEW software is developed to adjust the photopolymerization and photoinhibition irradiation parameters (e.g., exposure time, intensity, and pattern), and to control the build platform motion (e.g., layer thickness, stage speed).

To accomplish the envisioned two-wavelength PinPAM, the alignment of the two light sources is highly important to ensure precise inhibition and curing. In Appendix Section A, the method and result of aligning the two-wavelength projection in our PinPAM system are presented. Please note that the two-wavelength projection is not perfectly aligned (as illustrated in Appendix Section A), potentially introducing errors in printed geometry and diminishing the effectiveness of PinPAM. However, it’s crucial to note that this preliminary work primarily serves to illustrate the concept of PinPAM using a non-perfect system, showcasing its potential capabilities despite the observed misalignment. Addressing and refining such issues are anticipated in the development of an advanced PinPAM system.

2.2. Material system for PinPAM

We develop a PinPAM printable material system based on a literature formulation [31], which comprises photo inhibitors, photo initiators, and monomers as detailed below. The resin used in this work contains a mixture of 50 wt% Triethylene glycol dimethacrylate (TEGDMA) and 50 wt% bisphenol A glycidyl methacrylate (bisGMA) as monomers. Camphorquinone (CQ) is used as a blue light photo-initiator and ethyl 4-(dimethylamino)benzoate (EDAB) is added as a co-initiator. The 2,2′-Bis(2-chlorophenyl)-4,4′,5,5′-tetraphenyl-1,2′-biimidazole (o-Cl-HABI) is used as a UV light responsive photo inhibitor, which is dissolved in tetrahydrofuran (THF) as a 30 wt % solution before adding to the monomer mixture. The non-monomer mixture is formulated with 0.2 wt % CQ, 0.5 wt % EDAB and 3 wt% o-Cl-HABI. All the chemicals are purchased from Sigma-Aldrich. All the materials are used as received without any additional modifications.

2.3. Inhibition and curing characterization for a PinPAM material system

This section describes the methods employed and the results obtained in characterizing the inhibition zone thickness and the working curve of the model PinPAM material system (Section 2.2) using our PinPAM printer (Section 2.1).

First, for this special PinPAM process, it is important to know the inhibition zone characteristics, especially the inhibition zone thickness,

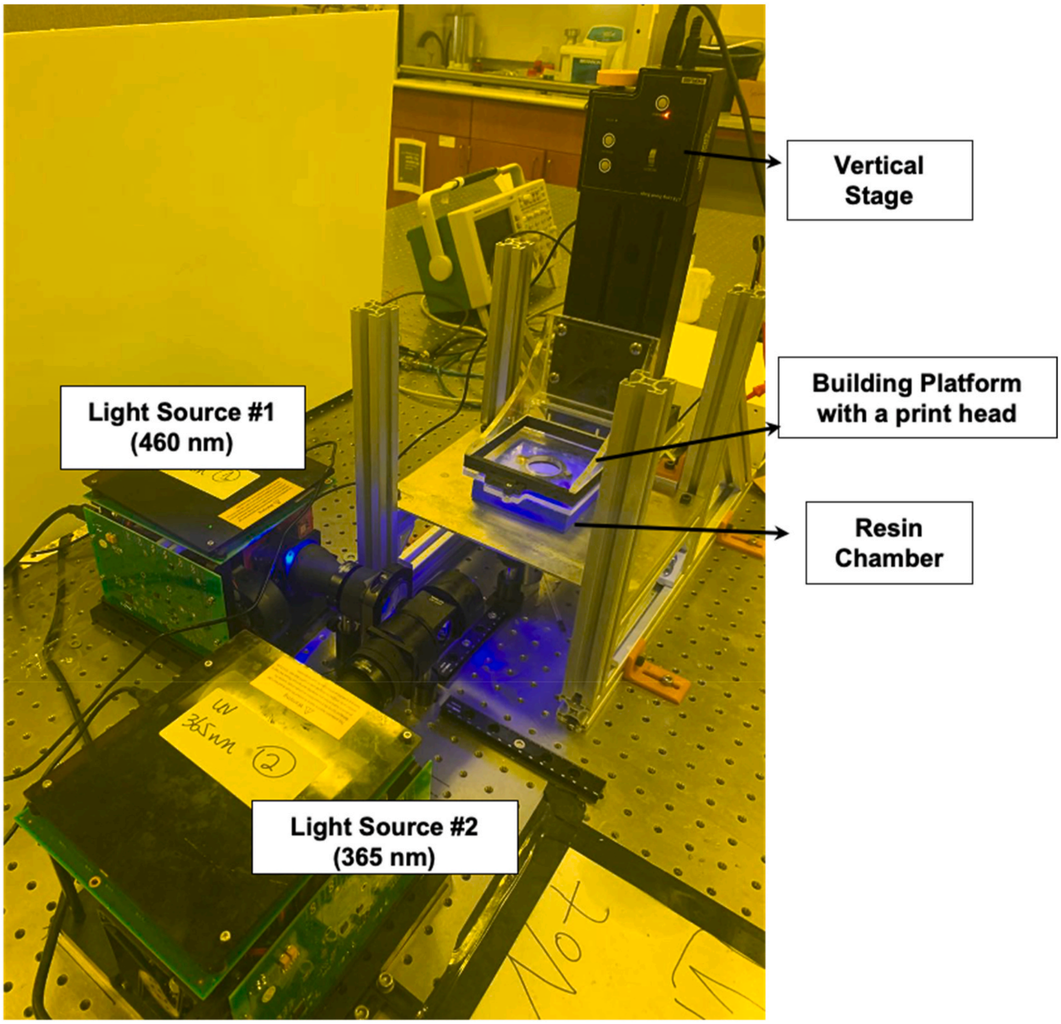

Fig. 1. In-house two-wavelength PinPAM system setup.

because it will directly affect the actual layer thickness. Note that the cured layer thickness in PinPAM is theoretically the user-specified layer thickness (the vertical stage's travel distance for each layer) minus the surplus of inhibition zone above the nominal print plane (i.e., the start position of the stage before printing the first layer). For the developed PinPAM material system (Section 2.2), an experiment is conducted to measure the inhibition zone thickness under varying ratios of UV light (for photoinhibition) and blue light (for photocuring) intensities. As illustrated in Fig. 2, to create a resin chamber for the inhibition zone characterization, a 0.8 mm thick spacer is first attached to a Teflon film positioned atop the projection window of the printer. Then, the resin is carefully pipetted and enclosed with a glass slide, after which the print stage is adjusted to make contact with and seal the chamber. Subsequently, the resin undergoes irradiation for 2 min under a constant blue curing light, with varying UV light intensities to attain different I_{UV}/I_{Blue} values.

To investigate the effect of curing light intensity on inhibition zone thickness, two sets of samples are cured at blue curing light intensities of 8.02 mW/cm^2 and 4.12 mW/cm^2, respectively. The inhibition-over-curing intensity ratio (I_{UV}/I_{Blue}) ranges from 0 to 0.98 in this

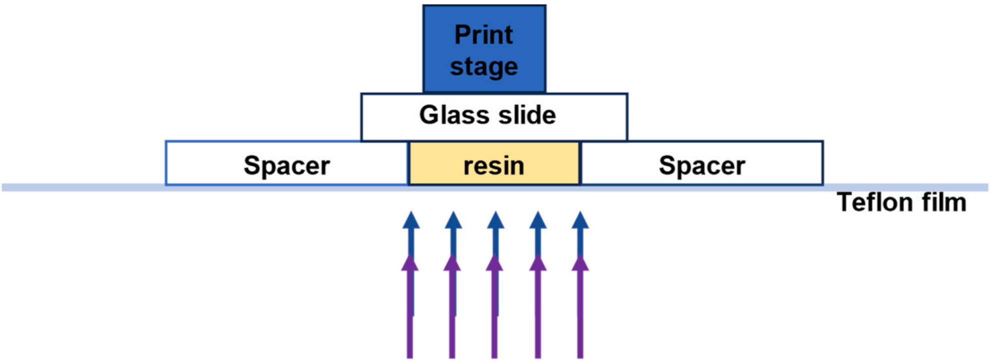

Fig. 2. Schematic setup for inhibition zone thickness characterization.

experiment. The cured sample is rinsed with isopropanol to remove any uncured resin and post-cured with blue light for an additional 2 minutes. The thickness of each sample cured under a different intensity ratio is measured using the caliper (precision ± 0.01 *mm*). The corresponding inhibition zone thickness is estimated by subtracting the measured sample thickness from the known spacer thickness.

Please note that the dynamic inhibition zone thickness in an actual PinPAM process may deviate from the presented inhibition zone thickness. The characterization provided here is based on a static curing experiment conducted in a small chamber with depleted photo inhibitors, resulting in limited inhibition power. We recommend evaluating the actual inhibition zone thickness through experimentation using a genuine PinPAM printing setup, which includes a build stage and a real-size vat of materials. While the simple static experiment can offer a reasonable estimate of the inhibition zone thickness, it is crucial to utilize the complete setup for accurate characterization. Furthermore, it is important to acknowledge that different material systems may exhibit varying inhibition curves. Therefore, a dedicated characterization experiment is essential to successfully implement PinPAM in diverse material scenarios.

Fig. 3 presents the inhibition characteristics of our PinPAM's material system. It indicates that the inhibition zone thickness increases with the inhibition-over-curing intensity ratio. At a blue curing light intensity of 4.12 mW/cm^2, the maximum intensity ratio I_{UV}/I_{Blue} achieved in our experiment is 0.98, resulting in an inhibition volume thickness of 0.43 mm. When the blue curing light intensity is increased to 8.02 mW/cm^2, the attainable maximum intensity ratio using our system is 0.51, and the corresponding inhibition volume thickness is 0.27 mm. Despite being cured with different curing light intensities, the inhibition volume thickness of the two sets of samples remains similar, especially at comparable values of inhibition-over-curing intensity ratios (e.g., 0.2, 0.3, and 0.5). Notably, as depicted in Fig. 3, at an intensity ratio (I_{UV}/I_{Blue}) of approximately 0.5, samples cured with higher blue light intensity (8.02 mW/cm^2) exhibit an inhibition volume thickness of 0.27 mm. The samples cured with lower blue light intensity (4.12 mW/cm^2) show a thickness of 0.21 mm. The blue markers (representing low blue light intensity) fall within the error bar range of the red marker (representing high blue light intensity). This suggests that the inhibition zone thickness for the two tested levels of blue light intensity shows no statistical significance, considering possible experimental errors. Furthermore, the experiment data are fitted as per Equation (1) [31], where I_{UV} and I_{Blue} are intensities of UV and blue light, β is inhibition coefficient, which is a constant for a specific resin formulation, and h_{uv} and h_{blue} are the absorption heights, calculated by the inverse of the sum of the product of concentrations of all absorbing species and their wavelength-specific absorptivity.

$$\textit{Inhibition volume thickness} = \frac{\ln\left(\frac{\beta I_{UV}}{I_{Blue}}\right)}{\frac{1}{h_{uv}} - \frac{1}{h_{blue}}} \tag{1}$$

Overall, the experimental findings above, demonstrating comparable inhibition zone thickness at similar intensity ratios and the well-fitted curves in Fig. 3, suggest a strong dependence of inhibition zone thickness on the inhibition-over-curing light intensity ratio (I_{UV}/I_{Blue}). Interestingly, these results indicate that the specific curing light intensity level, within the same material system, does not significantly impact the inhibition zone thickness. This observation aligns with the validation of Equation (1), which estimates the inhibition zone thickness based on the ratio I_{UV}/I_{Blue} (varied in the experiment) and material components' concentrations (assumed to be constant throughout the experiment). The agreement between the experimental outcomes and the equation supports the notion that the inhibition zone thickness is predominantly influenced by the inhibition-over-curing light intensity ratio (I_{UV}/I_{Blue}) rather than the absolute curing light intensity level in the context of the examined material system.

Moreover, using the same setup as in Fig. 2, the working curve for this material system is derived, as shown in Fig. 4. Jacobs' equation [33], represented by Equation (2), is used to fit the experimental data and determine the penetration depth D_p and critical exposure energy E_c. In this equation, C_d denotes the cured thickness, and E_0 represents the incident curing light exposure energy, calculated as the product of curing light intensity and exposure time [33]. For the specific material system in this work, the obtained values are $D_p = 0.64$ mm and $E_c = 238.53$ mJ/cm^2.

$$C_d = D_p \ln\left(\frac{E_0}{E_c}\right) \tag{2}$$

It is worth noting that the depth of penetration ($D_p = 0.64$ mm) characterized above exceeds the maximum inhibition zone thickness obtained (~0.42 mm as shown in Fig. 3). This disparity is necessary to ensure that the studied material can be effectively printed above the inhibition zone. The difference between D_p and inhibition zone thickness provides an estimate of the upper limit of layer thickness specified for a PinPAM process. Given the potential variability in inhibition zone

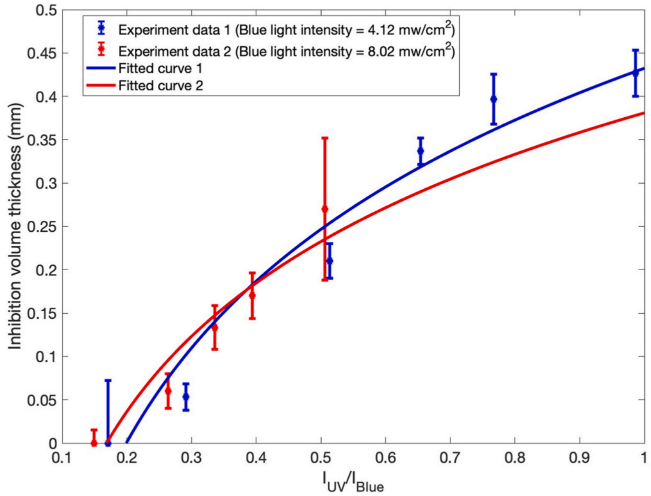

Fig. 3. Characterized inhibition zone thickness with the varying inhibition/curing intensity ratio (I_{UV}/I_{Blue}). (Note: each error bar represents the standard deviation of three replications.)

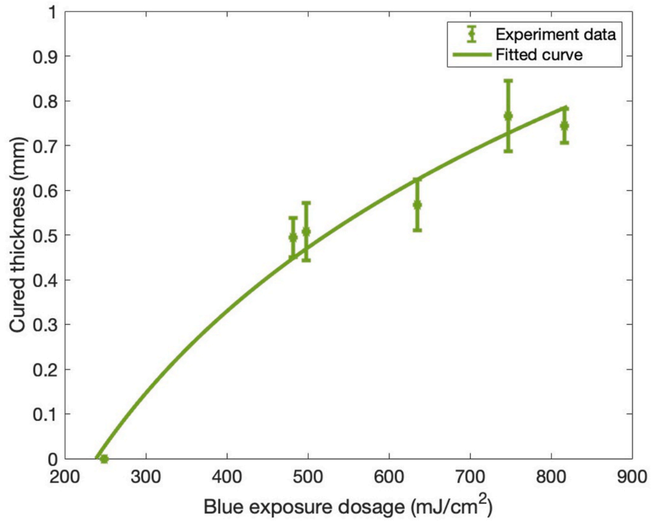

Fig. 4. Cured thickness versus blue light exposure dosage (Note: each error bar represents the standard deviation of three replications.). (For interpretation of the references to color in this figure legend, the reader is referred to the Web version of this article.)

thickness (up to hundreds of microns based on the characterization result in Fig. 3) attributed to the possibly changing inhibition-over-curing intensity ratio (I_{UV}/I_{Blue}), achieving precision geometry control in PinPAM necessitates adjusting the between-layer stage movement distance, typically equivalent to the nominal "layer thickness". In contrast, traditional VPP often overlooks oxygen inhibition variation, which could induce variation in inhibition zone thickness, typically on the order of tens of microns, and assumes that a constant layer thickness can be maintained by adopting a consistent stage travel distance for each layer printing.

In this initial study on PinPAM, a constant stage travel distance between layers, i.e., a nominal layer thickness of 50 μm, is employed in all the PinPAM experiments presented in subsequent sections. It's important to acknowledge that this simplification might introduce errors on the order of microns, in PinPAM part heights. These limitations will be addressed in future work.

3. Understanding the PinPAM process via experimental printing of pillar arrays

In this section, by printing samples with pillar arrays, we aim to demonstrate that geometry-aware photoinhibition, which adapts the inhibition parameters specifically to the curing zone and surrounding area, has a unique advantage of effectively tackling the over-curing issue, thus improving the part's three-dimensional accuracy and resolution. Specifically, we will focus on investigating the effects of inhibition patterning on PinPAM processes.

To begin, it's important to clarify the term "stationary PinPAM process" used in this work. This refers to a simplified PinPAM process that does not involve the movement of the print stage but focuses on constructing a basic geometry (e.g., a pillar with a constant cross-section) on the stationary print head. In Section 3.1, we initiate the examination of the impact of inhibition patterning on PinPAM through the stationary PinPAM process. Subsequently, we delve into a study on the more common and more complex PinPAM process, which entails the movement of the print stage, in the subsequent subsection (Section 3.2).

Given the prioritized need to tackle lateral over-curing in VPP, this section focuses on investigating the effects of the surrounding inhibition pattern parameters on lateral dimensions and resolution. Subsequent experiments utilize inhibition masks designed based on target cross-sectional profiles, comprising two primary sub-areas: overlapping with and surrounding the target curing region, respectively. The overlapping inhibition intensity I_o is calculated as the cure intensity I_{cure} multiplied by the overlapping inhibition ratio R_o, *i.e.*, $I_o = I_{cure} \times R_o$. Similarly, the surrounding inhibition intensity I_s calculated as $I_s = I_{cure} \times R_s$. It is worth noting that the overlapping and surrounding inhibitions could interact or interfere with each other due to chemical species diffusion and reaction kinetics, necessitating a more in-depth study of the complex inhibition pattern design and optimization in the future. Here, to specifically understand how the surrounding inhibition pattern parameters (e.g., intensity, shape) would affect the photopolymerized geometry, we conduct experimental pillar array printing using traditional VPP and PinPAM with no overlapping intensity (i.e., $R_o = 0$). Note that all the processes including the control group of the mimic of traditional VPP processes (i.e., non-inhibited VPP) use the same exposure curing parameters.

3.1. The effects of inhibition patterning on PinPAM that employs a stationary print stage

The stationary PinPAM experiment is executed utilizing a setup similar to that employed in the inhibition zone thickness characterization, as detailed in Section 2.3. However, a larger quantity of resin is employed to ensure the successful printing of a pillar array. The designed pillar array consists of 2 × 3 pillars, where each pillar has a target diameter of 2 mm and the distance between the center of adjacent pillars is 4 mm. The resin is irradiated for 1 min by a blue light mask with an intensity of $I_{cure} = 8.75 \text{ mW/cm}^2$, along with a UV light mask featuring various sizes and intensity values as shown in Table 1. The use of different UV inhibition masks aims to reduce over-curing and thus improve the dimensional accuracy of printed samples, particularly focusing on refining the diameters of the pillars within the designed array.

The images of printed samples are shown in Appendix Figure A-3. , while Table 1 provides a quantitative measurement of pillar diameters. The sample photos vividly depict that using only blue curing light (Sample 1) leads to expanded diameters and undesired connections between pillars due to pronounced lateral over-curing. Results from Samples 2–4 demonstrate that, with the same inhibition shape and size, a higher intensity ratio results in a reduced diameter for each pillar, indicating the inhibitory effect on print size. Moreover, Samples 4–6 reveal that, with the same inhibition-over-curing ratio but a larger ring size (measured by ring width), there is increased inhibition on curing (Sample 5 being the most under-cured due to over-inhibition). Samples 4 to 6 highlight that even with a relatively small intensity ratio (i.e., 0.09), over-curing can still be effectively reduced. From Tables 1 and it is evident that compared to Sample 1 (conventional VPP), Sample 6 printed by a PinPAM process with a near-optimal inhibition pattern achieves the best pillar diameter of 1.96 mm (closest to the target diameter of 2 mm). Furthermore, PinPAM yields a much smaller standard deviation within the array of pillar diameters (0.15 mm) than conventional VPP, indicating that PinPAM is a more uniform and precise process, better suited for printing precision structures such as pillar arrays than non-inhibited VPP processes. Meanwhile, it is crucial to emphasize the importance of developing and employing an optimal inhibition pattern, exemplified by the inhibition pattern utilized in printing Sample 6, to achieve accurate and precise prints with PinPAM.

3.2. The effects of inhibition patterning on PinPAM that involves a moving print stage

To explore the effects of inhibition patterns on PinPAM more comprehensively, this section focuses on practical PinPAM that involves the movement of the print stage. Two sets of samples are printed with varying numbers of layers – 50 layers and 25 layers, respectively. In both sets, the designed pillar diameter is 4 mm, and the distance between the center of adjacent pillars is 6 mm.

For Sample Set 1, 50 layers are printed, with a stage movement distance of 50 μm for each layer, thus the expected printed height is 2.5 mm. Table 2 shows the curing and inhibition exposure masks used for printing each sample, along with dimensional measurements of the corresponding pillar array. In the Appendix Figure A-4 Shows the images of the printed set of 50-layer samples, with red arrows indicating the height of unintended part connecting adjacent pillars, a consequence of lateral over-curing.

Firstly, in terms of vertical dimensions, Sample 1.1 produced by traditional VPP shows the lowest average pillar height of 1.45 mm, representing a 42 % deviation from the expected printed height of 2.5 mm. This discrepancy could be attributed to potential adhesion issues between the projection window and the print stage during printing, potentially leading to peeling of some parts from the sample. Comparatively, PinPAM-printed Samples 1.2 to 1.4 exhibit significantly fewer relative errors than Sample 1.1. This improvement may stem from the surrounding inhibition, contributing to a decrease in adhesion between the projection window and the print stage due to the diffusion of inhibiting species. As a result, a more accurate print height is achieved compared to Sample 1.1, where no inhibition is applied. However, the heights of Samples 1.2 to 1.4 all exceed the expected height (2.5 mm), suggesting the potential application of overlapping inhibition exposure directly beneath the curing zone. This could construct a more inhibitory dead zone, not only reducing the suction force between the part and vat substrate but also minimizing vertical over-curing. This aspect will be

Table 1

Experiment design and results of stationary PinPAM for printing a pillar array (Notes: 1. All masks are grayscale in the actual implementation of the PinPAM process; the curing mask is shown in blue and the inhibition mask is shown in purple only for visualization clarity. 2. Red highlights indicate the worst case arising from traditional non-inhibited VPP. 3. Green highlights indicate the best case resulting from near-optimal PinPAM that prints a pillar array with accurate and uniform diameters.).

Sample No.	Blue Light Curing Exposure Mask (Target pillar diameter: 2mm)	UV Light Inhibition Exposure Mask Pattern (Brighter color indicates greater inhibition intensity)	Inhibition Ring Width (mm)	*Inhibition-over-Curing Intensity Ratio* (I_{UV}/I_{Blue})	Printed Pillar Diameter (mm)	
					Average (Relative error)	Standard Deviation
1 (traditional VPP)	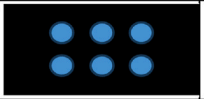	Purely Dark Image (No inhibition)	**0**	**0**	**2.4 (20%)**	**0.31**
2 (PinPAM)	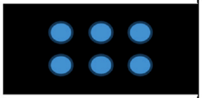	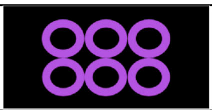	0.75	0.26	1.43 (-28.5%)	0.15
3 (PinPAM)	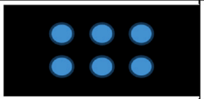	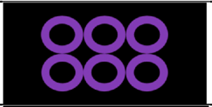	0.75	0.15	1.72 (-14%)	0.13
4 (PinPAM)	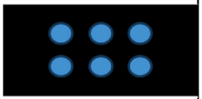		0.75	0.09	1.79 (-10.5%)	0.11
5 (PinPAM)	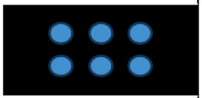		1	0.09	1.59 (-20.5%)	0.17
6 (PinPAM)	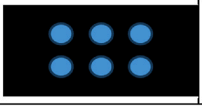	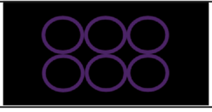	**0.5**	**0.09**	**1.96 (-2%)**	**0.15**

Table 2

Inhibition effects on PinPAM with a moving print stage: Experiment Set 1. (Notes: All masks are grayscale in the actual implementation of the PinPAM process; the curing mask is shown in blue and the inhibition mask is shown in purple only for visualization clarity.).

Sample No.	Blue Light Curing Mask (Target pillar diameter: 4 mm; height: 2.5 mm)	UV Light Inhibition Exposure Mask Pattern (Brighter color indicates greater inhibition intensity)	*Inhibition-over-Curing Intensity Ratio* (I_{UV}/I_{Blue})	Average pillar diameter at bottom (mm) (Relative Error)	Average pillar diameter at top (mm) (Relative Error)	Average pillar height (mm) (Relative Error)	Height of unwanted between-pillar connection due to over-cure (mm)
1.1 (traditional VPP)	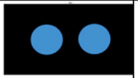	Purely Dark Image (No inhibition)	0	5.88 (47%)	4.78 (19.5%)	1.45 (-42%)	1.47
1.2 (PinPAM)	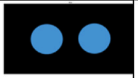	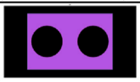	0.50	5.46 (36.5%)	2.90 (-27.5%)	2.65 (6.0%)	0.55
1.3 (PinPAM)	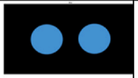	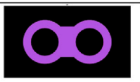	0.50	5.37 (34.3%)	3.19 (-20.3%)	2.66 (6.4%)	0.58
1.4 (PinPAM)	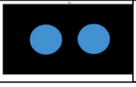	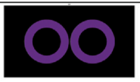	0.26	5.25 (31.3%)	3.45 (-13.8%)	2.83 (13.2%)	1.39

investigated further in Section 4, where both surrounding and overlapping inhibition patterns are employed to optimize the PinPAM process.

Concerning lateral shape and size, Sample 1.1 printed by traditional VPP exhibits the highest unwanted connecting part caused by lateral over-curing and the largest (most overcured) average pillar diameter at both the bottom and top. Samples 1.2 and 1.3, printed with a higher inhibition intensity ratio, show a reduction in overcured diameter and unwanted between-pillar connection resulting from lateral over-curing when compared to Sample 1.1 and Sample 1.4, both of which either have no inhibition or use a lower inhibition intensity ratio (I_{UV}/I_{Blue}). These observations highlight the potential of surrounding inhibition exposure to decrease lateral over-curing and enhance lateral dimensional accuracy and resolution. However, it is noteworthy that the inhibition pattern used in this set of experiments is not yet ideal for completely eliminating lateral over-curing. None of the processes in Sample Set 1 (Table 2) achieve target dimensions accurately or eliminate lateral over-curing entirely. For instance, the bottom diameters of the PinPAM samples are significantly larger than the target of 4 mm due to over-curing, while the top diameters are smaller than the target due to over-inhibition. These findings underscore the necessity of developing an adaptive inhibition pattern to achieve the target diameters and height, as well as reduce unwanted, overcured parts connecting adjacent pillars. This strategic approach is demonstrated in the subsequent experimental study with Sample Set 2.

For Sample Set 2, 25 layers are printed, with an expected print height of 1.25 mm. Table 3 details the two-wavelength exposure masks for the samples and provides corresponding measured dimensions. Fig. 5 showcases images of Sample 2.1 and Sample 2.2.

Similar to Sample 1.1 in Set 1, Sample 2.1 exhibits a lower-than-expected pillar height due to a relatively thin dead zone caused by oxygen inhibition and larger average diameters resulting from over-curing in traditional VPP. In contrast, employing a spatially adaptive inhibition pattern, as illustrated for Sample 2.2 in Table 3, PinPAM successfully eliminates the unintended overcured part between-pillar connections. This is achieved by utilizing a relatively high inhibition-over-curing intensity ratio (I_{UV}/I_{Blue}) of $R_{center} = 0.50$ in the space between adjacent pillars, as shown in the UV light exposure mask. A brighter color in the center area indicates that a higher inhibition light intensity is used there. Meanwhile, the PinPAM process significantly reduces the relative errors in the bottom and top diameters (4.03 mm at the bottom and 3.86 mm at the top) by employing a relatively lower intensity ratio (I_{UV}/I_{Blue}) of $R_{ring} = 0.15$ in the surrounding ring-belt area. However, neither sample in this experiment set reaches the expected height. Especially for Sample 2.2, still affected by vertical over-curing, the addition of an overlapping inhibition exposure to complement the surrounding inhibition exposure could be explored to address both lateral and vertical over-curing for achieving three-dimensional geometrical accuracy, as demonstrated in Section 4.

3.3. Need for spatiotemporally adaptive surrounding inhibition to accomplish PinPAM

Overall, this preliminary work reveals the significant need for tackling over-curing, especially in the lateral dimensions to improve overall geometrical accuracy and resolution. The results of PinPAM are promising with pronounced trends in reducing dimensional errors (e.g., pillar height and diameter), refining features (pillar edges), and improving resolutions (e.g., separating adjacent pillars), despite not perfectly achieving the target designs yet. This study strongly indicates and partially validates our hypothesis that adjusting the inhibition intensities surrounding and overlapping with the curing zone will lead to close conformance with the target designs, especially in terms of three-dimensional accuracy, shape retention, and resolution.

Essentially, the inhibition pattern in the context of PinPAM is a grayscale image serving as an optical mask that generates a spatial distribution of light intensities for comprehensive and localized inhibition. As observed in Section 3.2 using a constant inhibition intensity across layers could not achieve a uniform inhibition effect along the vertical direction. In Section 3.2, it has been demonstrated that using a constant inhibition intensity profile within a single layer does not yield as good effect as a spatially varying intensity profile. Therefore, varying inhibition intensity both laterally and vertically is needed to achieve optimal three-dimensional inhibition effect. This is due to the time-dependent and spatially varying distribution of inhibition and initiating species during VPP based AM, depending on the material properties (e.g., composition, viscosity), resin flow rheology, and part geometry. One potential solution is to develop a more sophisticated

Table 3

Inhibition effects on PinPAM with a moving print stage: Experiment Set 2 with spatially adaptive inhibition pattern. (Notes: 1. All masks are grayscale in the actual implementation of the PinPAM process; the curing mask is shown in blue and the inhibition mask is shown in purple only for visualization clarity. 2. Green highlights indicate the better-achieved results in the presented data.).

Sample No.	**Blue Light Curing Mask (Target pillar diameter: 4 mm; height: 1.25 mm)**	**UV Light Inhibition Exposure Mask Pattern (Brighter color indicates greater inhibition intensity;** R_{ring}, R_{center} is the Curing-over-Inhibition Ratio at the ring and center, respectively)	**Average pillar diameter at bottom (mm) (Relative Error)**	**Average pillar diameter at top (mm) (Relative Error)**	**Average pillar height (mm) (Relative Error)**	**Height of unwanted between-pillar connection due to over-cure (mm)**
2.1 (traditional VPP)	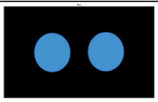	Purely Dark Image (No inhibition)	5.59 (39.8%)	4.21 (5.3%)	1.05 (-16.0%)	0.39
2.2 (PinPAM)	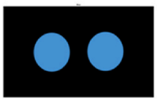	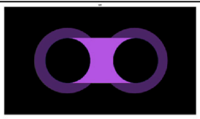 $R_{ring} = 0.15$, $R_{center} = 0.50$	**4.03 (0.8%)**	**3.86 (-3.5%)**	1.49 (19.2%)	**0**

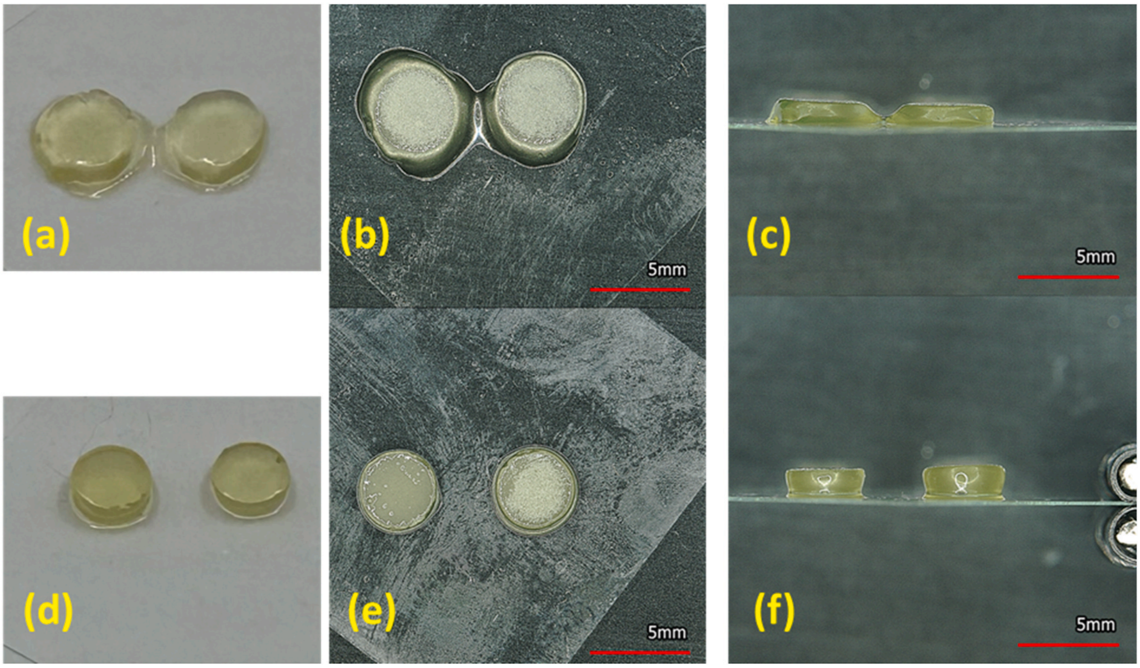

Fig. 5. The 25-layer samples in Experiment Set 2 were printed by conventional VPP (a–c) and PinPAM with adaptive inhibition pattern (d–f). From left to right: camera photo (a, d), and KEYENCE VR-3200 optical profilometer imaging, top view (b, e) and side view (c, f).

inhibition method using dynamic inhibition masks with a varying inhibition intensity profile that incorporates the effects of inhibition area, intensity level, and shape. Such adaptive inhibition masks will be aimed to consider the process dynamics for achieving uniform resolution and dimension accuracy within each layer and through all the layers. For example, higher inhibition intensity at the earlier layers and at the space among the pillars can be used in the demo case to help separate the pillars all the way through from the top down to the bottom. The envisioned adaptive inhibition strategy with optimal inhibition area, intensity, and shape is recommended to be developed in the future for establishing PinPAM.

As a further note on developing adaptive PinPAM, one should note the potential effect of the dynamical inhibition zone thickness, which is also pronounced in the current VPP process that relies on oxygen inhibition [34]. Based on Fig. 3, the inhibition zone thickness could vary between 0 and hundreds of microns. In our PinPAM experiment above, the initial position of the print head is constant. As the overlapping intensity ratio increases, the dynamic inhibition zone increases and thus reduces the actual layer thickness. Ideally, the print head should be placed on top of the dynamic inhibition zone. Therefore, to achieve more precise control of the vertical dimension, the position of the print head should be adjusted according to the corresponding layer's overlapping intensity ratio.

4. PinPAM process optimization to tackle over-curing: an initial study case

To address the issues identified in the previous section and to realize the full potential of PinPAM, here, using a simple geometry – a cylinder, we demonstrate how to design PinPAM process parameters, specifically the curing and inhibition light intensities, to attain desired sizes in all three dimensions (e.g., thickness, width). As a preliminary exploration, to simplify the process optimization problem, we fix the curing light intensity and aim to determine an optimal inhibition light intensity. This study case will shed light on the general process planning method for using PinPAM to fabricate other shapes and structures under various levels of curing light intensity.

4.1. Method of optimizing the PinPAM process

First, the PinPAM process planning is cast as a multi-objective optimization problem, which can be formulated mathematically as follows, to find an optimal combination of the surrounding inhibition ratio R_s and overlapping inhibition ratio R_o, which can minimize the errors in both vertical (height) and lateral (width, diameter, etc.) dimensions.

$$\min_{0\le R_s,R_o\le 1.5}\begin{cases} F_1(R_s,R_o)=|H-H_D|=|f_h(R_s,R_o)-H_D| \\ F_2(R_s,R_o)=|W-W_D|=|f_w(R_s,R_o)-W_D| \end{cases}$$

where, $R_s = I_{surrounding\_inhibit}/I_{cure}$, $R_o = I_{overlapping\_inhibit}/I_{cure}$, H: actual height of printed part; H_D: designed height; W: actual width (diameter in this case of cylinder sample); W_D: designed width (diameter).

As shown in Fig. 6, we design and implement a set of single pillar printing experiments by using blue light and UV light for curing and inhibition, respectively, with different combinations of R_s (0, 0.3, 0.6, and 0.9) and R_o (0, 0.4, 0.6, 0.8). The pillar's target dimensions are a height $H_D = 10$ mm, and a diameter $W_D = 4.5$ mm. Note the combination of $R_s = 0$ and $R_o = 0$ means no inhibition being applied to the VPP process, representing the traditional VPP process. The other combination of non-zero R_s and R_o represents the current literature practice of overlapping the inhibition zone with curing zone to increase dead-zone thickness thus print speed or pattern the topography (i.e., vertical thickness profile) [31].

To measure the dimensions of the samples, a caliper with a precision of ±0.01 mm is employed. For each combination of R_s and R_o, three replicates are printed under identical conditions to enhance the statistical reliability. Multiple measurements are conducted at various locations on each replicate, and the mean value of these measurements is utilized to determine the diameter and height of each replicate. The error between the measured values and designed values of each replicate is subsequently calculated. For each set of inhibition ratios, the average values of the three replicates are computed and utilized for Pareto optimization. Table A-1 shows a summary of error values for each combination of inhibition ratios.

The response surface method is employed to solve the multi-objective problem. The response surfaces method investigates the

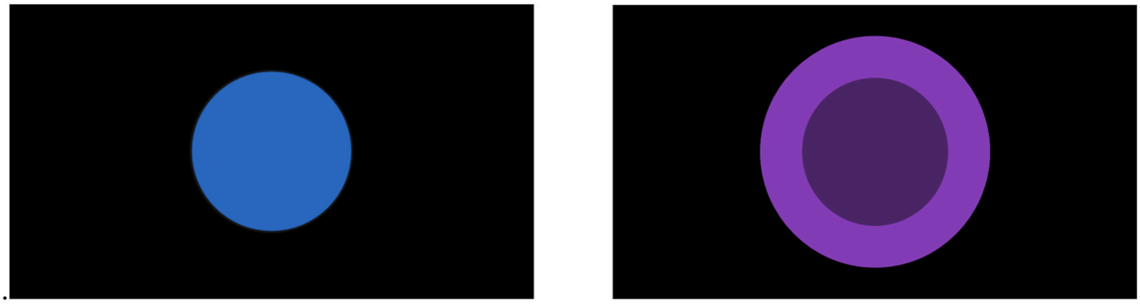

(a) (b)

Fig. 6. Projected optical masks during the PinPAM process of printing a single pillar. All masks are grayscale in the actual implementation of the PinPAM process; the curing mask is shown in blue and inhibition mask is shown in purple only for visualization clarity. (a) Curing mask of blue light circle. (460 nm, 8 mW/cm^2, diameter measured on the build plane: 4.5 mm). (b) Inhibition mask with a UV circle (365 nm, overlapping with the blue light circle in (a)) and a ring (circumferential to the curing circle). The UV light intensity is proportional to the grayscale of UV mask, with the grayscale 255 providing a maximal intensity of 12 mW/cm^2. Brighter color indicates greater inhibition intensity. (For interpretation of the references to color in this figure legend, the reader is referred to the Web version of this article.)

relationship between multiple variables and the objectives through a series of designed experiments, visualizing and evaluating trade-offs between different design objectives [35]. The response surface can identify the Pareto optimal front, which demonstrates a large number of optimal solutions to multi-objective optimization problems [36]. There is no single solution that optimizes all objectives concurrently for a nontrivial multi-objective problem. Therefore, there may exist many non-dominated solutions that are considered equally good. All the non-dominated solutions constitute Pareto front. From these Pareto optimum fronts, a compromise solution can be chosen based on specific objectives and preferences.

To explore the relationship between inhibition ratios and dimensional errors, the Curve Fitting Toolbox in MATLAB is used to perform the nonlinear regression of the experimental data (Table A-1 in Appendix Section C) using first-degree polynomial curve fitting. Details of the curve fitting results are shown in Appendix Section D. It is worth noting that the R-squared value for these two curve fitting functions is approximately 0.8, indicating that more experimental data could be collected to enhance the optimization model and obtain a more accurate estimation of the optimal inhibition process setting to accomplish PinPAM. With the fitted functions, the multi-objective optimization is solved using the Pareto search algorithm in MATLAB. The solved Pareto front is shown in Fig. 7.

In Fig. 7, the Pareto front displays many solutions that illustrate the trade-off between two objectives, and the corresponding inhibition ratios are shown in the Parameter Space. It can be observed that a Pareto solution with an index of 23 minimizes the error in both the lateral and vertical directions equally, which can be considered as the best solution for this problem. The corresponding inhibition ratios are $R_s = 0.11$ and $R_o = 0.56$. This could be quickly verified by examining the experimental data used in the curve fitting as shown in Table A-1 in Appendix Section C. Sample 9, which has inhibition values closer to the optimization results, shows lower error values compared to other samples.

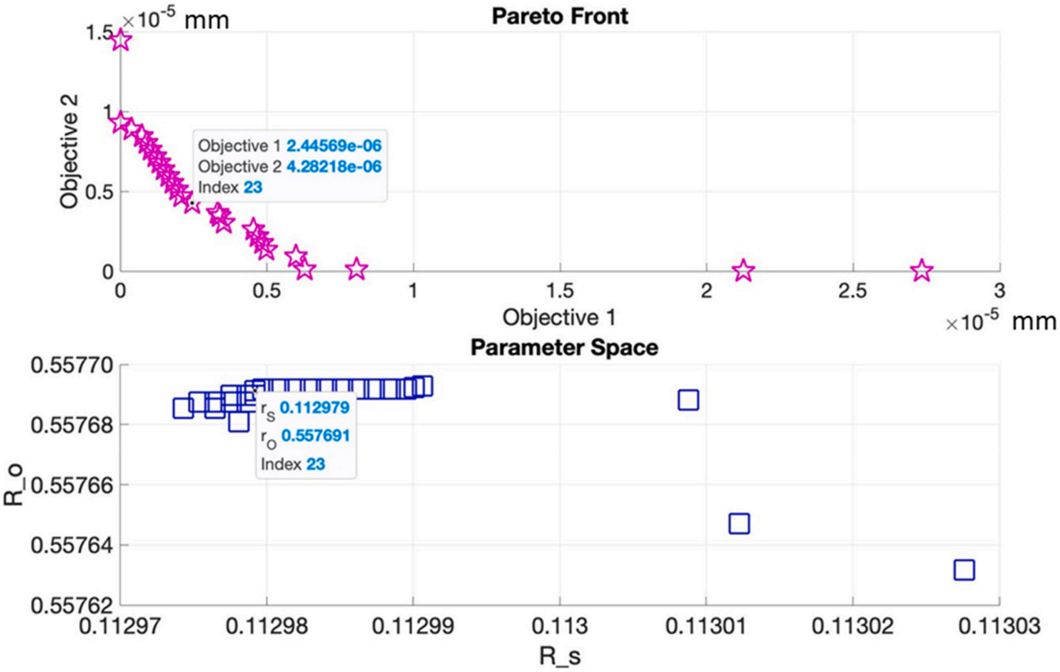

Fig. 7. Result of the Pareto optimization of PinPAM process parameters to increase dimensional accuracy in case of printing micropillars. Objective 1: minimize the vertical dimensional error. Objective 2: minimize the lateral dimensional error.

4.2. Experimental validation of the optimal PinPAM process setting

The optimal results could be further validated by conducting experiment using an estimated optimal setting determined in the previous section: $R_s{}^* = 0.11$ and $R_o{}^* = 0.56$.

First, as a counterexample, a non-optimal setting of $R_s = 0.3$, $R_o = 0.8$ was experimented with the printed sample as shown in Fig. 8. The sample on the left is measured to be 9.91 mm tall (−0.9 % error) and 4.9 mm in diameter (8.9 %), while the sample on the right side displays a height of 9.79 mm (−2.1 % error) and a diameter of 4.36 mm (−3.1 % error). Specifically, the higher-than-optimal values of R_s ($0.3 > R^* = 0.11$) and R_o ($0.8 > R_o{}^* = 0.56$) in this experiment yield under-cured height and diameter, thus resulting in negative errors as illustrated in Fig. 8. Overall, this experiment shows that the non-optimal PinPAM process setting may still be able to improve the accuracy to some extent, yet require a more suitable inhibition combination to obtain good accuracy in both the vertical and lateral dimensions.

Further, the optimal setting derived in the previous section was used to print a sample pillar. Due to the limited achievable grayscales (light intensities) in our DLP system, a set of inhibition ratios close to the optimal values ($R_s{}^* = 0.11$ and $R_o{}^* = 0.56$), $R_s = 0.15$, $R_o = 0.6$, were used to print the pillar. The resulting sample displays a height of 9.99 mm with a deviation of −0.01 mm and a relative error of −0.1 % and a diameter of 4.47 mm with a deviation of −0.03 mm and a relative error of −0.67 %, as shown in Fig. 9. Comparing this sample printed using the optimized inhibition ratios with the other samples as shown in Appendix Table A-1, we can see this is the best result with least errors in both vertical and lateral directions. Note that the optimized process printed sample outperforms the best sample in Table A-1 (i.e., Sample 9) specifically in reducing the lateral diameter error. Sample 9 essentially adopts overlapping inhibition only and has shown to be limited in confining the lateral over-curing. The comparison between our optimized PinPAM sample and Sample 9 that represents existing practice of VPP using photoinhibition [30–32] indicate that the state-of-the-art methods of simply using overlapping photoinhibition could be further improved by adding suitable (if not optimal) surrounding inhibition for tackling the lateral over-curing.

As a side note, for this pillar printing experiment, because of a recent adjustment of the optical system in our PinPAM machine, some faint blue light appeared in the surrounding area of the circle that was not originally designed for blue light exposure. During the printing, the unintentional faint blue light exposure energy accumulated to the threshold curing energy, thus curing the resin and resulting in a tale not by design. It is sort of extrinsic over-curing caused by the projection system flaws, different from the intrinsic over-curing caused by the VPP process itself. Nevertheless, to counteract this additional blue light exposure, we applied an inhibiting UV mask to block the unwanted blue light irradiation and successfully printed a sample without the tail. This unexpected experience provides additional proof of PinPAM being able to tackle unwanted over-curing, intrinsic or extrinsic. It also shows the agility of PinPAM in shaping the printed parts by modifying the inhibition pattern according to the actual optical system performance.

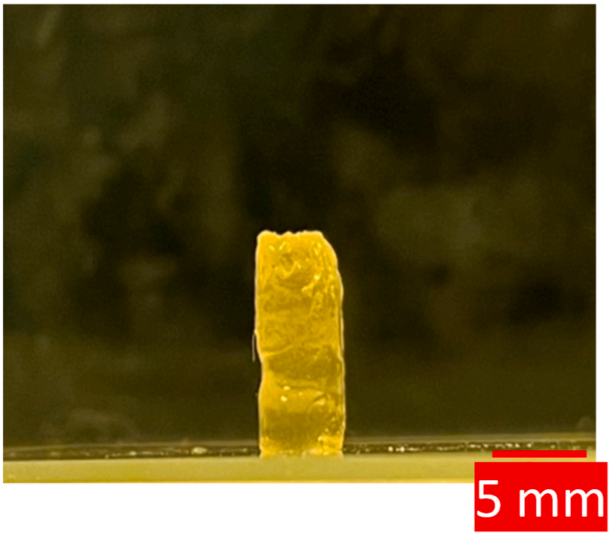

Fig. 9. Printed pillar using PinPAM with optimized overlapping and surrounding inhibitions: $\boldsymbol{R_s} = 0.15$, $\boldsymbol{R_o} = 0.6$. (Note: Slightly different perspectives lead to variations in the target geometry boundary as outlined in Figs. 8 and 9.)

In summary, the PinPAM process optimization primarily depends on the optical mask projection system's ability to project the desired light intensities accurately. In this work, it is important to note that only a near-optimal setting, affected by some unintended blue light exposure, was implemented in our experiment due to limitations in our projection light source and optical setup, which could not project the exact optimized blue and UV light intensity values. This issue could potentially be resolved by utilizing a more precisely engineered optical system. Overall, a reliable and robust projection system is one of the key factors contributing to the accuracy of the process. Moreover, it should be noted that the optimization was based on a limited set of experimental data. Collecting more experimental data would be beneficial in achieving truly optimal two-wavelength exposure profiles, thereby enhancing the performance of PinPAM.

5. Cosnclusion

In this work, we develop a geometry-aware adaptive photoinhibition scheme to enhance the cross-sectional profile on a layer basis, thus improving the overall 3D part geometric accuracy. The proposed

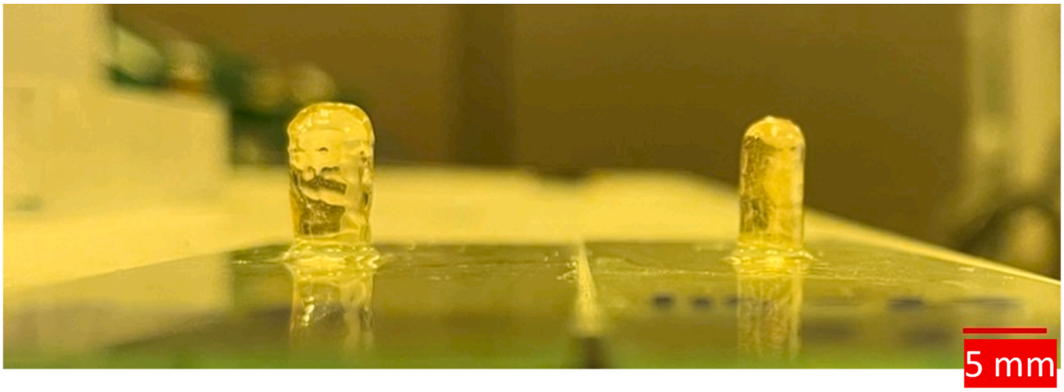

Fig. 8. Representative samples of printed pillar using (Left) a curing mask only as in conventional VPP, and (Right) the same curing mask but with an inhibition mask that provides overlapping and surrounding inhibitions: $\boldsymbol{R_s} = 0.3$, $\boldsymbol{R_o} = 0.8$, as in this new PinPAM process.

PinPAM method is based on the hypothesis that a sequence of layer-wise inhibition patterns, each comprising inhibition regions overlapping with and surrounding the target curing area and characterized by a spatial distribution of inhibition intensity, can be optimized to achieve dimensional accuracy and resolution in both vertical and lateral directions.

We first evaluate the inhibition and curing characteristics of an exemplary PinPAM material system and conduct preliminary experiments to understand PinPAM process-structure relationships. We demonstrate a proof-of-concept study for the future development of the proposed PinPAM process by printing pillar array samples that require both accuracy and resolution. The results show that the diameter error in a single-cylinder printing drops from 8.9 % in a typical VPP process to −3.1 % in PinPAM, achieving an error of −0.67 % in the optimized PinPAM. This indicates that PinPAM can tackle the over-curing issue and needs to be optimized to fulfill its promise. Comparisons between the conventional single-wavelength exposure mask projection-based VPP and our PinPAM show that PinPAM can effectively prevent lateral over-curing and enhance lateral resolution while maintaining good accuracy in vertical thickness.

To further develop the PinPAM process, several directions could be pursued. More complex optimization problems could be formulated to vary spatiotemporally both the curing light pattern and inhibition light pattern to print heterogeneous parts for applications such as soft robots and metamaterials. Additional properties, such as the degree of curing, will be incorporated as objectives in the PinPAM process optimization problem for geometrical accuracy and mechanical strength. Advanced optimization algorithms, such as neural networks and improved response surface methods, will be developed to design the inhibition pattern parameters. Substantial chemistry and material research is needed to develop suitable photoinhibition materials for different photopolymer resins. Multiphysics modeling and simulation, coupled with in-situ monitoring techniques like in-situ interferometry and ultrasonic methods [37,38], can be used to elucidate the PinPAM mechanism. This approach will enable a more effective optimization of inhibition pattern parameters, while also facilitating the fundamental studies of chemistry and material system design for PinPAM. Besides, for future implementation, inter-layer stage movement or layer thickness should be adjusted in real-time according to the dynamical inhibition/curing intensity ratio.

To conclude, this pilot study demonstrates a new paradigm of VPP underpinned by the idea of PinPAM, which uses inhibition to achieve high-fidelity photopolymerized parts with improved dimensional accuracy, enhanced resolution, and smaller feature size. The promise of PinPAM can be accomplished by optimal design of layer-wise inhibition patterns, akin to the research field of support structure design for existing AM processes. The PinPAM process opens up a new avenue for VPP-based AM, useful in applications that demand geometrical accuracy or resolution for achieving special functionalities, such as 4D printing.

CRediT authorship contribution statement

Yue Zhang: Writing – review & editing, Writing – original draft, Visualization, Methodology, Investigation, Data curation. **Heyang Zhang:** Writing – review & editing, Software, Investigation, Data curation. **Xiayun Zhao:** Writing – review & editing, Writing – original draft, Supervision, Project administration, Funding acquisition, Conceptualization.

Declaration of competing interest

The authors declare the following financial interests/personal relationships which may be considered as potential competing interests:

Xiayun Zhao reports financial support provided by the National Science Foundation Faculty Early Career Development Program under Award ID CMMI-2238557.

Xiayun Zhao has a pending patent with US Application No.: 17/437,343. International Application No.: PCT/US20/21,727. The reported photoinhibition aided photopolymer additive manufacturing system and method along with some of the discussions have been filed within the pending patent above.

Xiayun Zhao reports a relationship with University of Pittsburgh that includes employment.

Acknowledgments

This material is based upon the work supported by the National Science Foundation Faculty Early Career Development program (CAREER Award: CMMI-2238557). Any opinions, findings, and conclusions or recommendations expressed in this publication are those of the authors and do not necessarily reflect the views of the National Science Foundation. The authors would also like to thank Dr. Chaitanya Krishna Prasad Vallabh and Zekun Wu for their work on the in-house system setup in the ZIP-AM lab.

Appendix

A. Two-wavelength light source alignment

For the alignment of the two WinTECH PRO-6500 LED projectors (wavelengths 460 nm and 365 nm), which are combined through a 50-50 beam splitter, an FLIR camera (Model BFS–U3–120S4M) is used. The camera is placed at the location of the print stage. The image intensities of the two projectors are lowered using software control and neutral density filters to an acceptable level that prevents overexposure of the camera sensors. The optics and projectors are then adjusted so that the projection is focused on the camera.

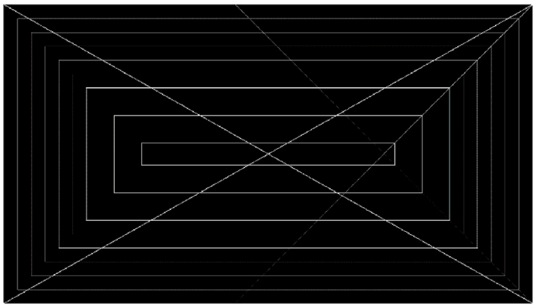

Fig. ure A-1. Custom alignment test pattern

The alignment involves adjusting the positions of the LED module as well as the projection lens until the images projected are overlapping and have the same size. Images of a custom alignment projection, shown in Figure A-1 and a built-in rectangular grid test pattern are projected and recorded. The images are then post-processed so that the intensities of the images are normalized.

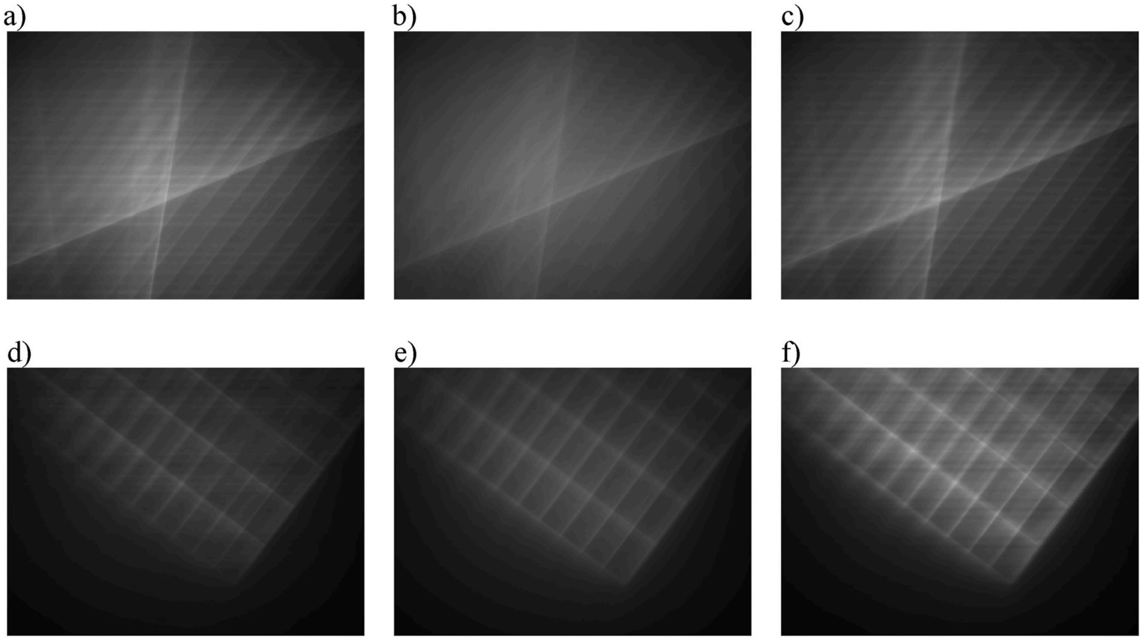

Fig. ure A-2. The imaging of custom alignment image (custom) of (a) UV (b) Blue (c) Both light sources. And built-in test image (grid) of (d) UV (e) Blue (f) Both

Then, the images are compared using the UQI (Universal Quality Image Index) algorithm[1] for its tolerance for the difference in contrast and intensity that is difficult to remove using the pre-processing algorithms. The UQI index is on a scale of 0–1, the alignment image is rated 0.939, the grid image is rated 0.968.

B. Experiment results of inhibition patterning for PinPAM processing

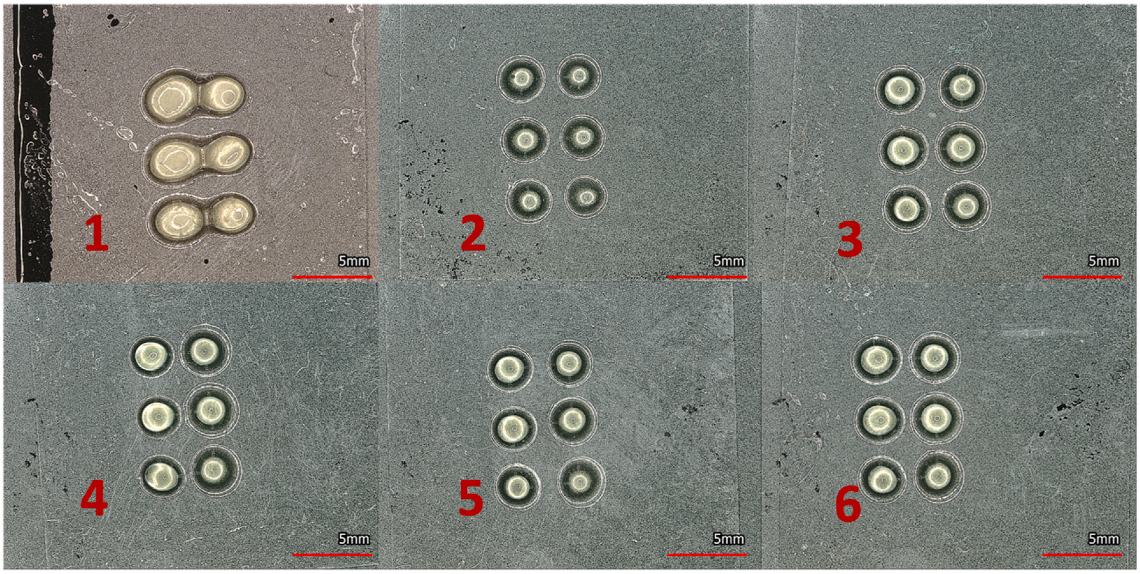

Fig. ure A-3. KEYENCE VR-3200 optical profilometer images of the pillar array samples printed using different UV inhibition masks in Section 3.1

---

[1] Zhou Wang and A. C. Bovik, "A universal image quality index," in IEEE Signal Processing Letters, vol. 9, no. 3, pp. 81–84, March 2002, https://doi.org/10.1109/97.995823.

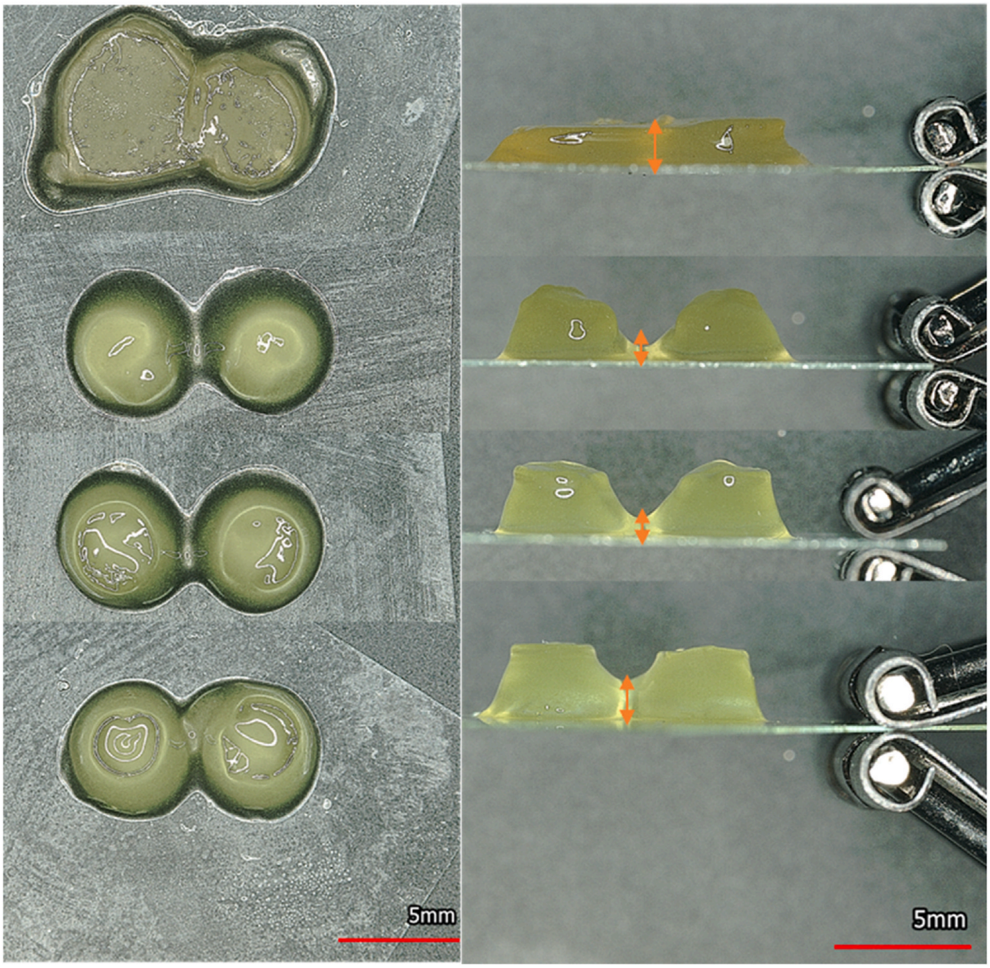

Fig. ure A-4. KEYENCE VR-3200 optical profilometer images of the printed 50-layer samples in Section 3.2: Samples 1 to 4 from top to bottom: top view (Left) and side view (right). The red arrow indicates the height of the unwanted between-pillar connection due to lateral over-curing.

C. Experimental data for the PinPAM process optimization

Table A-1 lists the data used in a demo case of PinPAM process optimization in Section 4. The optimal setting is estimated to be $R_s = 0.11$ and $R_o = 0.56$. This can be quickly verified by the sample data shown in Table A-1. Sample 9, which has inhibition values close to the optimization results show lower error values than other samples.

Table A-1
Experimental data used in the PinPAM process optimization

Sample	R_s (ratio of Surrounding Inhibition and Curing Intensities)	R_o (ratio of Overlapping Inhibition and Curing Intensities)	Diameter error: average diameter - designed diameter (mm)	Thickness error: average thickness - designed thickness (mm)
1	0	0	0.40	0.48
2	0.3	0	0.05	0.22
3	0.6	0	−0.08	0.20
4	0.9	0	−0.11	0.02
5	0	0.4	0.13	0.10
6	0.3	0.4	0.02	0.13
7	0.6	0.4	−0.19	0.03
8	0.9	0.4	−0.03	0.05
9	0	0.6	0.09	0.01
10	0.3	0.6	−0.18	−0.14
11	0.6	0.6	−0.24	−0.07
12	0.9	0.6	−0.35	−0.10
13	0	0.8	−0.12	−0.16
14	0.3	0.8	−0.14	−0.29
15	0.6	0.8	−0.30	−0.21
16	0.9	0.8	−0.36	−0.10

D. Curve Fitting Results in the PinPAM Process Optimization

Height error function

```
Linear model Poly11:
f(x,y) = p00 + p10*x + p01*y
Coefficients (with 95% confidence bounds):
p00 =      0.3105  (0.193, 0.4281)
p10 =     -0.1375  (-0.2925, 0.01746)
p01 =     -0.5289  (-0.7046, -0.3532)
Goodness of fit:
SSE: 0.1204
R-square: 0.7795
Adjusted R-square: 0.7456
RMSE: 0.09623
```

Result: f1(x,y)=0.3105-0.1375*x-0.5289*y, where x= r_c, y= r_o

Width error function

```
Linear model Poly11:
f(x,y) = p00 + p10*x + p01*y
Coefficients (with 95% confidence bounds):
p00 =      0.2575  (0.1435, 0.3715)
p10 =     -0.3842  (-0.5344, -0.2339)
p01 =     -0.3839  (-0.5543, -0.2135)
Goodness of fit:
SSE: 0.1132
R-square: 0.8065
Adjusted R-square: 0.7768
RMSE: 0.09333
```

Result: F2(x,y)= 0.2575 -0.3842*x -0.3839*y, where x= r_c, y= r_o

References

[1] report 3D printing and additive manufacturing state of the industry annual worldwide progress report. Fort Collins, CO: Wohlers Associates; 2017.

[2] Caudill C, Perry JL, Iliadis K, Tessema AT, Lee BJ, Mecham BS, Tian S, DeSimone JM. Transdermal vaccination via 3D-printed microneedles induces potent humoral and cellular immunity. Proc Natl Acad Sci USA 2021;118(39).

[3] Andreu A, Su P-C, Kim J-H, Ng CS, Kim S, Kim I, Lee J, Noh J, Subramanian AS, Yoon Y-J. 4D printing materials for vat photopolymerization. Addit Manuf 2021; 44:102024.

[4] Han D, Morde RS, Mariani S, La Mattina AA, Vignali E, Yang C, Barillaro G, Lee H. 4D printing of a bioinspired microneedle array with backward-facing barbs for enhanced tissue adhesion. Adv Funct Mater 2020;30(11):1909197.

[5] Huanga C, Quinnb D, Suresh S, Hsiaa KJ. Controlled molecular self-assembly of complex three-dimensional structures in soft materials. Proc Natl Acad Sci USA 2018;115(1):70–4.

[6] Saleh Ehab, Zhang Fan, He Yinfeng, Vaithilingam Jayasheelan, Fernandez Javier Ledesma, Wildman Ricky, Ashcroft Ian, Hague Richard, Dickens Phill, Tuck C. 3D inkjet printing of electronics using UV conversion. Advanced Materials Technologies 2017;2(10):1700134.

[7] Lis M, Plaut M, Zai A, Cipolle D, Russo J, Lewis J, Fedynyshyn T. Polymer dielectrics for 3D-printed RF devices in the ka band. Advanced Materials Technologies 2016;1(2):1600027.

[8] Tumbleston JR, Shirvanyants D, Ermoshkin N, Januszewicz R, Johnson AR, Kelly D, Chen K, Pinschmidt R, Rolland JP, Ermoshkin A, Samulski ET, DeSimone JM. Continuous liquid interface production of 3D objects. Science 2015; 347(6228):1349–52.

[9] Shusteff M, Browar AEM, Kelly BE, Henriksson J, Weisgraber TH, Panas RM, Fang NX, Spadaccini CM. One-step volumetric additive manufacturing of complex polymer structures. Sci Adv 2017;3(12).

[10] Naik DL, Kiran R. On anisotropy, strain rate and size effects in vat photopolymerization based specimens. Addit Manuf 2018;23:181–96.

[11] Lalevée J, Fouassier J-P. Photopolymerisation initiating systems. Royal Society of Chemistry; 2018.

[12] Shusteff M. Volumetric additive manufacturing of polymer structures by holographically projected light fields, department of electrical engineering and computer science. Massachusetts Institute of Technology; 2017.

[13] McGregor DJ, Tawfick S, Kin WP. Mechanical properties of hexagonal lattice structures fabricated using continuous liquid interface production additive manufacturing. Addit Manuf 2018.

[14] Gittard SD, Nguyen A, Obata K, Koroleva A, Narayan RJ, Chichkov BN. Fabrication of microscale medical devices by two-photon polymerization with multiple foci via a spatial light modulator. Biomed Opt Express 2011;2(11):3167–78.

[15] Kelemen L, Ormos P, Vizsnyiczai G. Two-photon polymerization with optimized spatial light modulator. J Eur Opt Soc: Rapid Publications 2011;6.

[16] Lin Y, Gao C, Gritsenko D, Zhou R, Xu J. Soft lithography based on photolithography and two-photon polymerization. Microfluid Nanofluidics 2018; 22(97).

[17] Sugioka K, Matsuda T, Ito Y. Photofabrication, photochemistry for biomedical applications. Singapore: Springer; 2018. p. 51–82.

[18] Bourdon L, Maurin J-C, Gritsch K, Brioude A, Salles V. Improvements in resolution of additive manufacturing: advances in two-photon polymerization and direct-writing electrospinning techniques. ACS Biomater Sci Eng 2018;4(12):3927–38.

[19] de Miguel G, Vicidomini G, Harke B, Diaspro A. Linewidth and writing resolution, three-dimensional microfabrication using two-photon polymerization. 2016. p. 190–220.

[20] Bártolo P. Stereolithography: materials, processes and applications. 2011.

[21] Zakeri S, Vippola M, Levänen E. A comprehensive review of the photopolymerization of ceramic resins used in stereolithography. Addit Manuf 2020;35:101177.

[22] Zhang R, Larsen NB. Stereolithographic hydrogel printing of 3D culture chips with biofunctionalized complex 3D perfusion networks. Lab Chip 2017;17(24):4273–82.

[23] Ahn D, Stevens LM, Zhou K, Page ZA. Rapid high-resolution visible light 3D printing. ACS Cent Sci 2020;6(9):1555–63.

[24] Gong H, Beauchamp M, Perry S, Woolley AT, Nordin GP. Optical approach to resin formulation for 3D printed microfluidics. RSC Adv 2015;5(129):106621–32.

[25] Zheng X, Deotte J, Alonso MP, Farquar GR, Weisgraber TH, Gemberling S, Lee H, Fang N, Spadaccini CM. Design and optimization of a light-emitting diode projection micro-stereolithography three-dimensional manufacturing system. Rev Sci Instrum 2012;83(12):125001.

[26] Pritchard ZD, Beer MP, Whelan RJ, Scott TF, Burns MA. Modeling and correcting cure-through in continuous stereolithographic 3D printing. Advanced Materials Technologies 2019;4(12).

[27] Guven E, Karpat Y, Cakmakci M. Improving the dimensional accuracy of micro parts 3D printed with projection-based continuous vat photopolymerization using a model-based grayscale optimization method. Addit Manuf 2022;57.

[28] Xu Y, Qi F, Mao H, Li S, Zhu Y, Gong J, Wang L, Malmstadt N, Chen Y. In-situ transfer vat photopolymerization for transparent microfluidic device fabrication. Nat Commun 2022;13(1):918.

[29] Zhou C, Chen Y, Waltz RA. Optimized mask image projection for solid freeform fabrication. J Manuf Sci Eng 2009;131(6).

[30] Li F, Thickett SC, Maya F, Doeven EH, Guijt RM, Breadmore MC. Rapid additive manufacturing of 3D geometric structures via dual-wavelength polymerization. ACS Macro Lett 2020:1409–14.

[31] De Beer MP, van der Laan HL, Cole MA, Whelan RJ, Burns MA, Scott TF. Rapid, continuous additive manufacturing by volumetric polymerization inhibition patterning. Sci Adv 2019;5(1):eaau8723.

[32] van der Laan HL, Burns MA, Scott TF. Volumetric photopolymerization confinement through dual-wavelength photoinitiation and photoinhibition. ACS Macro Lett 2019:899–904.

[33] Jacobs PF. Rapid prototyping & manufacturing: fundamentals of stereolithography. 1992.

[34] Lee BJ, Hsiao K, Lipkowitz G, Samuelsen T, Tate L, DeSimone JM. Characterization of a 30 microm pixel size CLIP-based 3D printer and its enhancement through dynamic printing optimization. Addit Manuf 2022;55.

[35] Deb K. Multi-objective optimisation using evolutionary algorithms: an introduction. In: Wang L, Ng AHC, Deb K, editors. Multi-objective evolutionary optimisation for product design and manufacturing. London: Springer London; 2011. p. 3–34.

[36] Goel T, Vaidyanathan R, Haftka RT, Shyy W, Queipo NV, Tucker K. Response surface approximation of Pareto optimal front in multi-objective optimization. Comput Methods Appl Mech Eng 2007;196(4–6):879–93.

[37] Zhang Y, Zhang H, Zhao X. In-situ interferometric curing monitoring for digital light processing based vat photopolymerization additive manufacturing. Addit Manuf 2024;81.

[38] Vallabh CKP, Zhang Y, Zhao X. In-situ ultrasonic monitoring for Vat Photopolymerization. Addit Manuf 2022;55:102801.